

<sup>1</sup> **Three-Dimensional Morphometry of Ooids in Oolites**

<sup>2</sup> **Bolton Howes<sup>1</sup>, Akshay Mehra<sup>1,2</sup>, Adam Maloof<sup>1</sup>**

<sup>3</sup> <sup>1</sup>Department of Geosciences, Princeton University, Guyot Hall, Washington Road, Princeton, NJ 08544,  
<sup>4</sup> USA  
<sup>5</sup> <sup>2</sup>Department of Earth Sciences, Dartmouth College, Hanover, NH, 03755, USA

6      **Abstract**

7      The prevalence of ooids in the stratigraphic record and their well-established associa-  
 8      tion with shallow-water carbonate environments make ooids an important paleoenviron-  
 9      mental indicator. Studies of modern ooids in Turks and Caicos and The Bahamas have  
 10     demonstrated that the size and shape of ooids depend on the depositional environment  
 11     and peak water velocity. These findings suggest that we can leverage the morphology  
 12     of ooids in ancient oolites as indicators of depositional environment and paleohydraulic  
 13     conditions. Currently, researchers measure the size and shape of lithified ooids on two-  
 14     dimensional surfaces (i.e. thin sections or polished slabs), which often requires researchers  
 15     to assume the random 2D slice intersects the center of the ooid, and that the ooid is spher-  
 16     ical. Here we demonstrate that this assumption is rarely true, and results in errors of  
 17     up to 35% on measurements as simple as major axis length. Accurate measurement of  
 18     the size and shape of ooids in a lithified sample requires that the measurements be made  
 19     on three dimensional reconstructions. We present a method for making 3D reconstruc-  
 20     tions by serial grinding and image processing. Our method accurately measures the size  
 21     (axes lengths, volume, and surface area), shape (prolateness and oblateness), and growth  
 22     history of individual ooids within an oolite, as well as the sorting and porosity of the sam-  
 23     ple. The ability to extract these measurements from an oolite means we can use the re-  
 24     lationship between ooid morphology, depositional setting, and hydraulic conditions de-  
 25     termined from studies of modern carbonate platforms as a tool for understanding an-  
 26     cient carbonate environments.

27      **1 Introduction**

28      Ooids are concentrically-laminated carbonate grains that are abundant in shallow-  
 29      water carbonate environments spanning the Archean to the Modern. The prevalence of  
 30      ooids in shallow-water carbonate rocks, and the narrow depth range of their formation  
 31      (Geyman & Maloof, 2018; Harris et al., 2019), make ooids a particularly valuable pa-  
 32      leoenvironmental proxy and a stable frame of reference for comparing carbonate plat-  
 33      forms throughout Earth's history. Carbonate platforms contain a mosaic of subenvirons-  
 34      ments (facies) like oolitic shoals, beaches, lagoons, tidal channels, etc. Each of these en-  
 35      vironments has unique chemical and physical conditions, which produce ooids with facies-  
 36      dependent sizes and shapes (Figure 1a&b; Mariotti et al. (2018); Trower et al. (2018)).  
 37      Consequently, the morphology of ooids and their lamellae can be used to refine facies mod-  
 38      els of ancient carbonate platforms and improve paleoenvironmental reconstructions.

39      While some features of ooid growth remain mysterious, there is general agreement  
 40      that ooids grow from the precipitation of calcium carbonate onto the surface of a sus-  
 41      pended nucleus or an existing ooid (Bathurst, 1972). The ooid continues to grow until  
 42      it is either buried, too big to be transported (Sumner & Grotzinger, 1993), or precip-  
 43      itation and abrasion rates reach a dynamic equilibrium (Figure 1c; Trower et al. (2017)).  
 44      This model provides a useful heuristic for understanding the relationship between en-  
 45      vironmental conditions and ooid size by indicating that increased precipitation rates and  
 46      more frequent ooid transport lead to larger ooids.

47      Like size, the shape of the ooid reflects the conditions under which the ooid formed.  
 48      The shape of an ooid is the product of collisions during saltation and friction with the  
 49      substrate, which produce spherical and flattened shapes respectively (Domokos & Gib-  
 50      bbons, 2012; Sipos et al., 2018). Based on the shape evolution model of ooids described  
 51      by Sipos et al. (2018), spherical ooids should become elongated if the primary transport  
 52      mode changes from saltation to bed-load transport. An ooid's lamellae preserve the his-  
 53      tory of an ooid's shape as it grows. This growth history may contain information about  
 54      how sediment transport changes as the grain size—and mass—increases (Heller et al.,  
 55      1980). Understanding how transport mode changes as a function of size can provide clues  
 56      about paleohydraulic conditions of ooid-forming environments and perhaps elucidate the

57 formation of giant ooids, which must have formed under uniquely saturated and/or turbulent  
 58 conditions to reach their size (Heller et al., 1980; Sumner & Grotzinger, 1993; Sipos  
 59 et al., 2018; Trower, 2020).

60 Lithified ooids typically have the same composition and physical properties as the  
 61 binding cement, precluding measurement through physical separation or x-ray computed  
 62 tomographic techniques. The inability to make 3D measurements has forced researchers  
 63 to measure the size and shapes of ooids on polished surfaces and in thin sections. Previous  
 64 research has demonstrated that it is not possible to accurately characterize 3D size  
 65 and shape distributions from 2D measurements (DeHoff, 1983; Mehra & Maloof, 2018).  
 66 We expand on those results by presenting synthetic experiments with spherical and el-  
 67 lipsoidal shapes, demonstrating that estimates of 3D morphology from measurements made  
 68 on a 2D cross section can be highly inaccurate (Figure 2). To overcome the limitations  
 69 of 2D measurements, we serially ground, imaged, and segmented oolites using the Grind-  
 70 ing, Imaging, and Reconstruction Instrument (GIRI) at Princeton University (Mehra &  
 71 Maloof, 2018), resulting in quantitative 3D reconstruction that enable accurate measure-  
 72 ment of ooid size and shape.

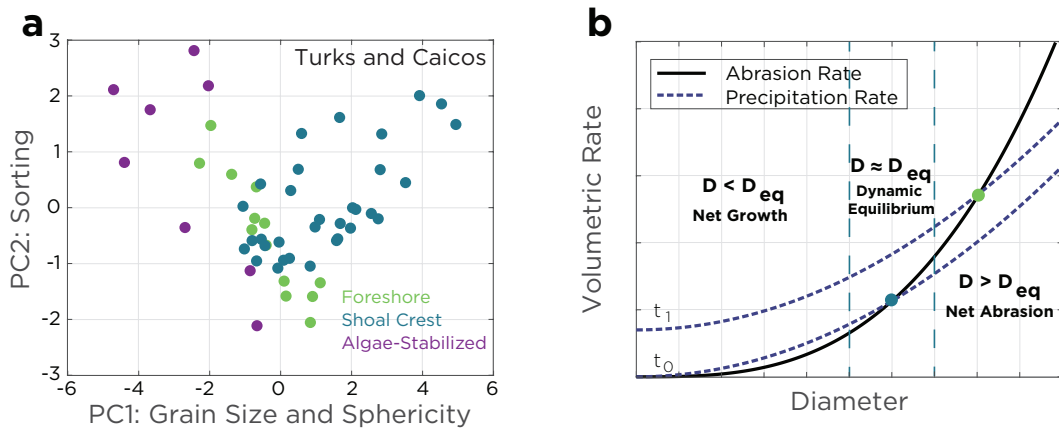


**Figure 1.** (a) Principal component analysis (PCA) of the size and shape of modern ooids from the Turks and Caicos demonstrates that the morphometry of ooids is facies dependent Trower et al. (2017). (b) Carbonate saturation state and the hydraulic conditions determine the size of an ooid. For example, if the precipitation rate increases (as seen in the upward shift from  $t_0$  to  $t_1$ ), the precipitation rate also will increase and the ooid will reach a new equilibrium size (light green dot). Modified from Trower et al. (2017).

## 73 2 The necessity of 3D Measurements

74 The limitation measurements from thin sections and polished slabs is that these  
 75 measurements represent 2D apparent dimensions instead of 3D grain dimensions. The  
 76 two central problems with making 2D measurements on 3D objects are the cut-section  
 77 effect, which arises because a grain is seldom cut exactly through its center, and the inter-  
 78 section probability effect, because a 2D slice is more likely to intersect a large grain  
 79 than a small one (Higgins, 2000). These problems can be partially addressed by apply-  
 80 ing stereological corrections to the 2D slices (Peterson, 1996; Sahagian & Proussevitch,  
 81 1998; Higgins, 2000), but these solutions require assumptions about several parameters  
 82 of the sample including the size distribution type (e.g. log-normal), particle shape, and  
 83 sorting of the rock. In the case of ooids in an oolite, shape and sorting are parameters  
 84 we need to know in order to deduce environment (Figure 1a&b), so we cannot make these

assumptions. Furthermore, these assumptions may not be valid for ooids. For example, ooids within the same layer can be many different shapes, so assuming a single particle shape for stereological analysis would be inappropriate. Here we quantify the errors associated with 2D measurements, and then present a method for directly measuring the size and shape distribution of ooids in an oolite from a 3D reconstruction.

## 2.1 Size Errors in 2D

Even simple size distributions of spherical and ellipsoidal grains are difficult, if not impossible, to accurately describe from 2D measurements. The measurement of the diameter of a population of grains with a normally-distributed major axis length shows that the 2D apparent size underestimates the true size distribution (Figure 2a&b). For spheres in this experiment, the error is solely due to the cut-section effect. In ellipsoids, the error associated with 2D measurements arises from the cut-section effect as well as intersections that are nearly perpendicular to the major axis mistaking the major and intermediate axes (Figure 2c). Similarly, attempts to measure the intermediate axis are complicated by both the cut-section effect and mistaking the minor axis for the intermediate axis when the intersection is nearly perpendicular to the intermediate axis (Figure 2d). Error from 2D measurements of the major axis of an ellipsoid increases as the ellipsoid becomes less spherical, especially as the ellipsoid becomes more prolate (Figure 2e), reaching 35% when the major axis is twice as long as the intermediate axis. For ooids with an aspect ratio similar to those from Turks and Caicos (Trower et al., 2018), we expect errors of 15%, which means 85% of the samples would have indistinguishable D50 values (50th percentile of grain diameters). This error would preclude identification of depositional environments based on ooid shape and size because it is the most heavily weighted variable in PC1 from the PCA in Figure 1. In an attempt to overcome the cut-section effect, it is common practice for researchers to measure only ooids they believe are cut through the nucleus, but we demonstrate that while this technique is better, there are still errors of up to 30% depending on the size of the nucleus and the shape of the ooid (Figure 2f), not to mention the difficulty in identifying an ooid's nucleus (Figure 3a–d). The reader should note that these experiments only account for the cut-section effect, so they can be considered minimum-error scenarios.

## 2.2 Shape Errors in 2D

Just as with size, 2D apparent dimensions provide inaccurate approximations of 3D shape. For example, we consider a single synthetic ooid with five growth lamellae and measure the prolateness of the ellipsoid represented by each lamellae with 2500 random intersections of the ooid (Figure 3d). Even if we only include the planes that intersect all five growth bands, the resulting estimate of prolateness (intermediate axis length divided by long axis length) for a single lamination varies by up to 30%, and the percent error of the median measurement is wrong by up to 13.9% (3e; this error strongly depends on the shape of the growth band as in Figure 2e&d). The random cuts also demonstrate that when an ooid has well-preserved lamellae, it is difficult to determine when a plane truly cuts through the nucleus, which is consistent with natural samples (Figure 3a–d). In Figure 3d, all of the random slices appear to intersect a nucleus, but only because they are synthetic and with a known number of lamellae can we determine which are cut through the nucleus. Additionally, some ooids have obvious nuclei (like a shell or fragment of another ooid), but these nuclei can have irregular or elongated shapes and there will be substantial error from missing the center of the nucleus (Figure 7c). Combined, these problems with 2D measurements of ooid lamellae demonstrate that studies of ooid shape and growth history require 3D reconstructions.

133 **2.3 Porosity Errors in 2D**

134 Accurate porosity estimates are crucial for understanding the potential of a rock  
 135 for both oil extraction and CO<sub>2</sub> sequestration, as well as modeling interstitial fluid flow.  
 136 Just as 2D sections are unreliable recorders of size and shape (Figure 2), individual 2D  
 137 sections are also unable to accurately describe porosity. For instance, when estimating  
 138 porosity by measuring the area of every grain and void space on 1000 random sections  
 139 through an oolite, any one estimate can be up to 30% wrong (Figure 4a). Error will in-  
 140 crease when measuring only a subset of grains on each sample (e.g., via point counting).  
 141 Additionally, while an average of multiple sections can approximate volumetric poros-  
 142 ity, a large number of measurements are required to achieve high accuracy: in the syn-  
 143 synthetic example, it takes 77 fully segmented slices to be within 5% of the true porosity  
 144 value for the volume, and 273 slices to be within 1% of the true value (Figure 4b).

145 **3 Materials and Methods**146 **3.1 Making 3D Measurements**

147 To make direct measurements in 3D, we serially ground and imaged an oolite col-  
 148 lected from Jouster's Cay, Andros Island, The Bahamas. The sample is a lightly-cemented  
 149 oolite associated with aeolian coastal dunes formed near an active oolitic shoreface (Halley  
 150 & Harris, 1979). There are 30  $\mu\text{m}$  between images, and the pixel size in each image is  
 151 5.6  $\mu\text{m}$ . For complete details of the grinding and imaging routine see Mehra and Mal-  
 152 loof (2018). The sample contains 847 slices and over 30,000 ooids, each individually seg-  
 153 mented and measured via an image processing pipeline.

154 **3.2 Image Processing**

155 Segmenting and measuring of 3D granular particles is a challenging task and an  
 156 active field of research in computer vision, material sciences, and biology (Jaquet et al.,  
 157 2013). The difficulty arises from needing to separate objects of the same material with  
 158 a high degree of connectivity—or that have grown together like ooids cemented by cal-  
 159 cium carbonate. The first step is to identify all the ooid and non-ooid pixels in an im-  
 160 age, for which we used a convolutional neural network (CNN). Using the tracing tools  
 161 in Dragonfly ORS (Object Research Systems, Inc, n.d.), we built a training dataset by  
 162 tracing over 1.25 million pixels of the ooid and 500,000 of the non-ooid class out of a dataset  
 163 of ~2 billion pixels (Figure 5b). These training pixels are on ten different images distributed  
 164 throughout the image stack. We then used these training data to train a CNN, which  
 165 labelled every pixel as either ooid or not ooid (Figure 5c). Isolating individual ooids for  
 166 measurement required implementing a watershed, which consists of finding the distance  
 167 of every ooid-labelled pixel to the nearest non-ooid labelled pixel (Figure 5d), using the  
 168 regional maximum distance as the “seeds” for the watershed (Figure 5e). Morpholog-  
 169 ical measurements use the Euclidean distance between neighbor voxels and the center  
 170 structuring element, so we transformed the initial 5.6 x 5.6 x 30  $\mu\text{m}$  voxels to 10 x 10  
 171 x 10  $\mu\text{m}$  voxels to remove anisotropy from the dataset. This technique is common prac-  
 172 tice in 3D imaging techniques like x-ray computed tomography (Pierret et al., 2002; Capowiez  
 173 et al., 2003). Complete MATLAB code for the CNN and the specifications for the wa-  
 174 tershed in Avizo (a scientific visualization software package) are provided in the supple-  
 175 ment.

176 **3.3 Measurements**

177 Ooid size measurements were made individually on each ooid in MATLAB using  
 178 the built in `regionprops3` function, which provides measurements of the principal axis  
 179 lengths, volume, and surface area. From these measurements it is possible to derive shape  
 180 and sorting metrics. All particles with a long axis length shorter than 100  $\mu\text{m}$  or longer

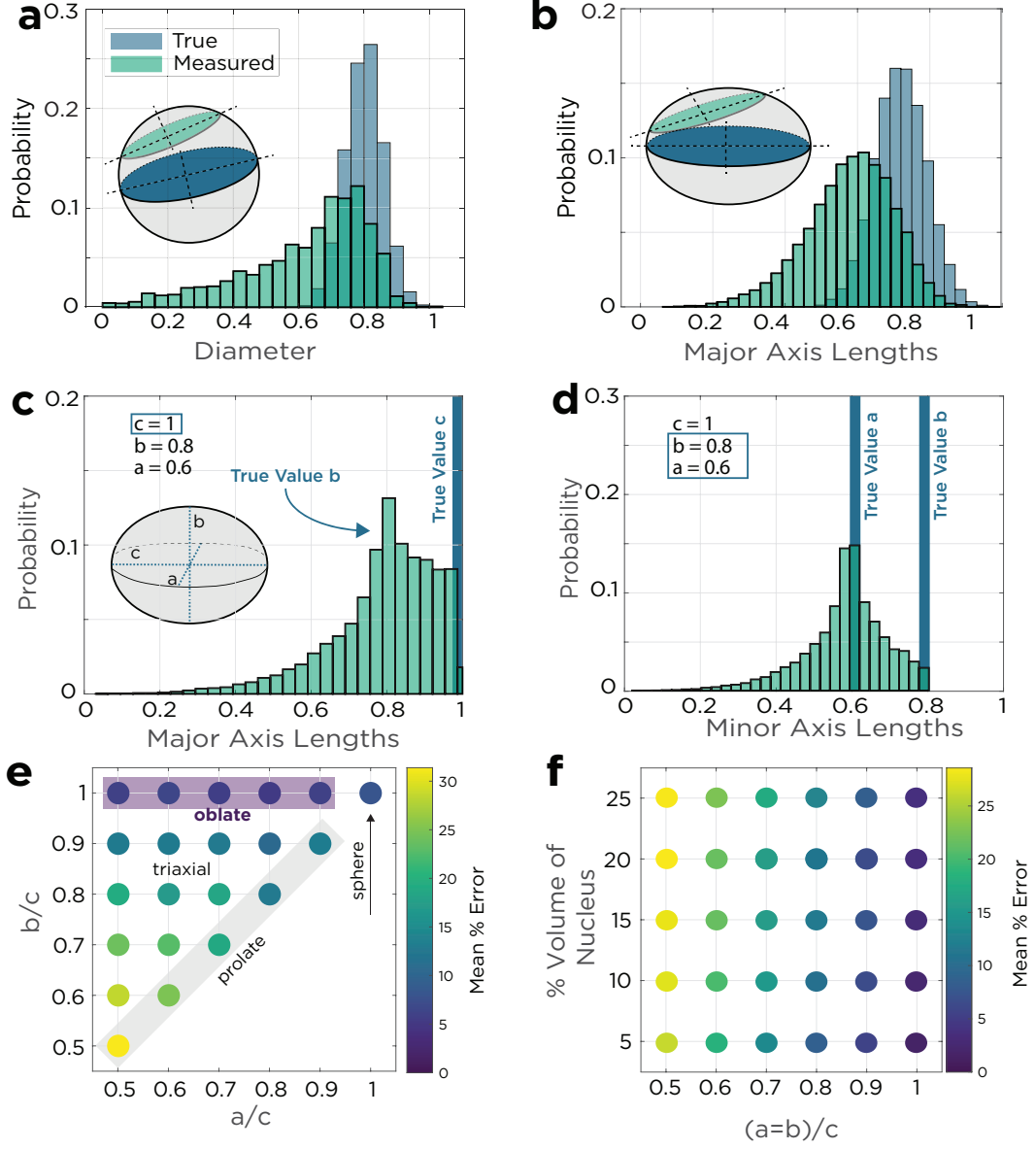


**Figure 2.** (a) The difference between the diameter of a population of spheres and the major axis length measured on cut spheres from the same population demonstrates that 2D cuts of a sphere underestimate the true size distribution of the population. (b) The difference between the true major axis length of population of ellipsoids ( $a/c = 0.6, b/c = 0.8$ ) and the major axis lengths measured on a random cut through ellipsoids from this distribution. (c) Measurement of the major axis,  $c$ , of a single ellipsoid on a random 2D slices underestimates the major axis length. (d) Measurement of the minor axis of the ellipse formed by a random intersection with an ellipsoid leads to error in the estimation of the minor axes. (e) Each dot represents the mean percent error of the median of 100 measurements of the major axis length for a range of ellipsoid shapes. The mean error increases as the ellipsoids become less spherical and more prolate. (f) Mean percent error of the median of 100 measurements of the long axis on a plane that intersects the nucleus as a function of prolateness and the size of the nucleus. Error increases as the size of the nucleus increases and as grain becomes less spherical.

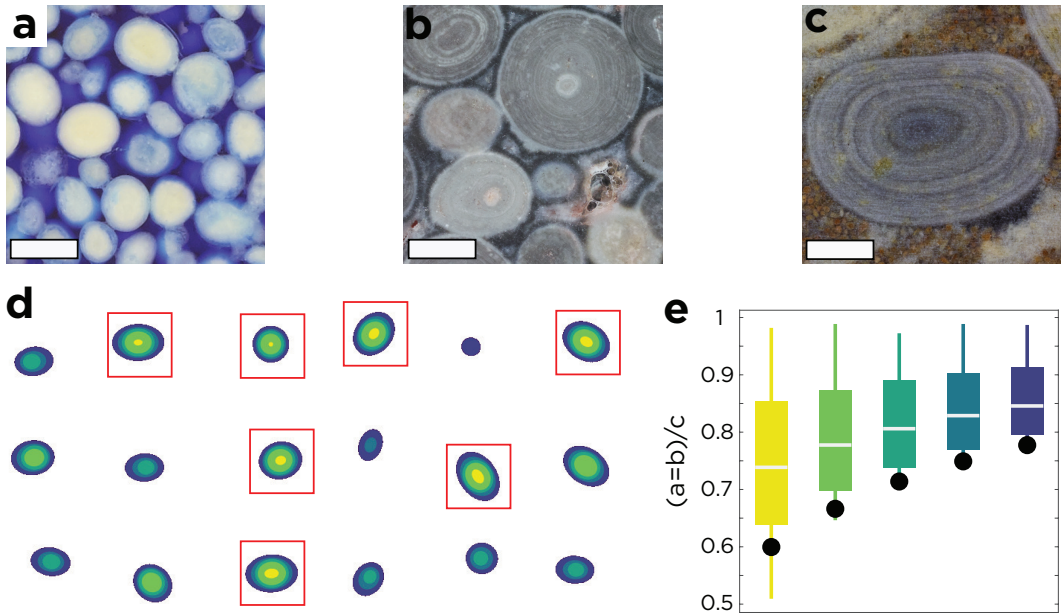


**Figure 3.** (a) Holocene oolite from Joulter’s Cay, The Bahamas. White scale bar is  $100\ \mu\text{m}$  (MacLennan et al., 2018). (b) Giant ooids from the Tonian Matheos Formation of Ethiopia. White scale bar is  $0.5\ \text{cm}$ . (c) Giant ooids from the Etina Formation in Australia. White scale bar is  $0.5\ \text{cm}$  (Rose et al., 2013). (a–c) These photographs demonstrate the difficulty of identifying the nucleus of an ooid from a 2D slice through an oolite. In (a), there are no clear nuclei in any of the ooids, In (b) and (c), banding of the ooids make it appear as if the cut is through the nucleus even though our 3D models reveal that none of the ooids present are actually cut through their nucleus in these slices. (d) 12 of the 2500 random cuts through a synthetic ellipsoidal ooid with five lamellae show the many different cross sections that can be produced from slicing a single ellipsoid. The red boxes outline slices that intersect all five lamellae. (e) The box plot shows the distribution of apparent prolateness values produced from 2D slices of the ooid in (d), and only slices that intersect the nucleus are used to calculate these distributions. From left to right in (e), the error of the median is 13.9%, 11.1%, 9.2%, 7.2%, and 6.8%. Two-dimensional slices overestimate how spherical the ooids are because many slices are oblique or perpendicular to the c-axis producing more circular cross-sections. The colors of the box plots match the colors of the lamellae in (d). Black dots mark the true flattening value for the lamellae.

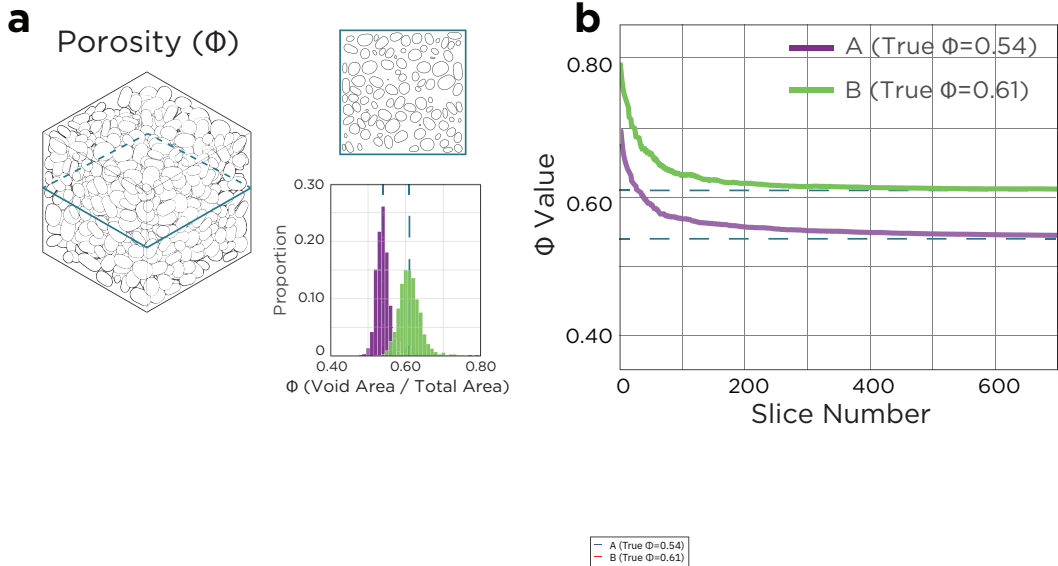


**Figure 4.** (a) Measurement of porosity in an oolite based on 2D intersections leads to a distribution of porosity estimates (purple represents a perfectly-packed volume of grains with a log-normal distribution; green is the same as purple, but with randomly added void space throughout the volume). (b) Convergence on the accurate estimate requires the measurement of tens to hundreds of fully-segmented slices.

than 750  $\mu\text{m}$  were removed to filter out non-ooloid particles like shells and grapestones. In total, this process takes 5–6 days per sample: 3–4 days to grind and image, 3–4 hours to make a training dataset, then train the neural network and segment the images overnight, then a day for any necessary post-processing. The grinding and imaging is completely automated (Mehra & Maloof, 2018), and the training and post-processing can be optimized when there are multiple samples with similar colors and textures because you can reuse the segmentation model and post-processing routines.

### 3.4 Joulter's Cay Measurements

Analysis of the ooids in the Joulter's Cay image stack demonstrates the image processing routine can provide measurements of individual ooids in a lithified oolite (Figure 6a). Since the ooids in the lithified oolite were sourced from the nearby shoreface; we can compare the size of the ooids from the image processing routine to modern ooids collected from the Joulter's Cay shoreface measured with a camsizer and see that they are similar (Figure 6b). We expect the lithified eolianite to show improved sorting over the source shoreface, which is observed: the Joulter's Cay sample has a sorting of 0.70, which is better sorted than any of the 22 ooid samples from a 1 km transect of the nearby shoreface, and is 48% better than the average shoreface ooid sample on the northern part of Andros Island (sorting is measured using a normalized dispersion parameter,  $\sigma^* = \frac{d_{50}-d_{90}}{d_{50}}$ ). Additionally, the error in size estimate would be approximately 20% for ooids with the a/c and b/c ratio of those in the Joulter's Cay sample based on the simulations in Figure 2f. This lack of accuracy and precision in size estimates from 2D measurements along with errors from the intersection probability effect, would have prevented differentiating between eolian and submarine environments without the three-dimensional reconstruction. Additionally, with the fully-segmented image stack we are able to measure the porosity of the oolite: 59.6% (Figure 6c–d).

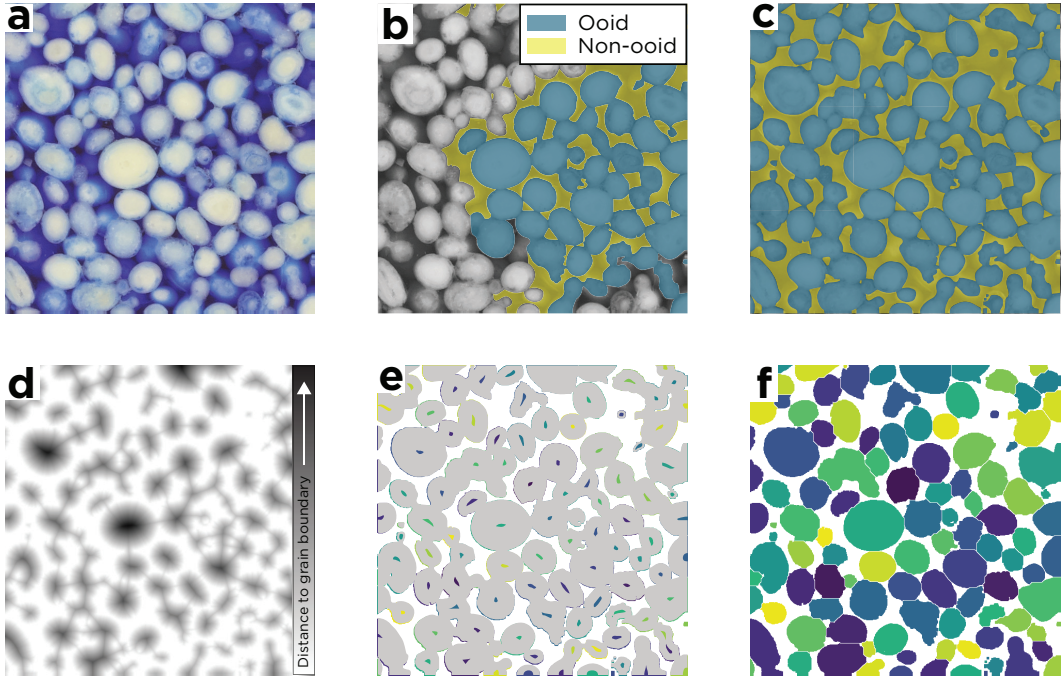


**Figure 5.** (a) The segmentation process uses the red channel because red provides the greatest contrast with the blue, pore-filling epoxy that was used to prevent plucking during grinding. (b) We create a training mask by tracing over an image, which then is used to train a CNN. Pixels in the ooid class are blue and pixels in the non-ooid class are yellow. (c) An image classified by the CNN (d) The euclidean distance of each ooid-labelled pixel from the nearest non-ooid pixel. Darker color means the distance is greater. (d) We filtered out local distance maxima by using the extended-maxima transform (colored blobs) to seed the watershed, and masked out the rest of the ooid pixels (gray). (f) After the watershed transform, all ooids are individually labelled and ready for measurement. White bar is 1 mm.

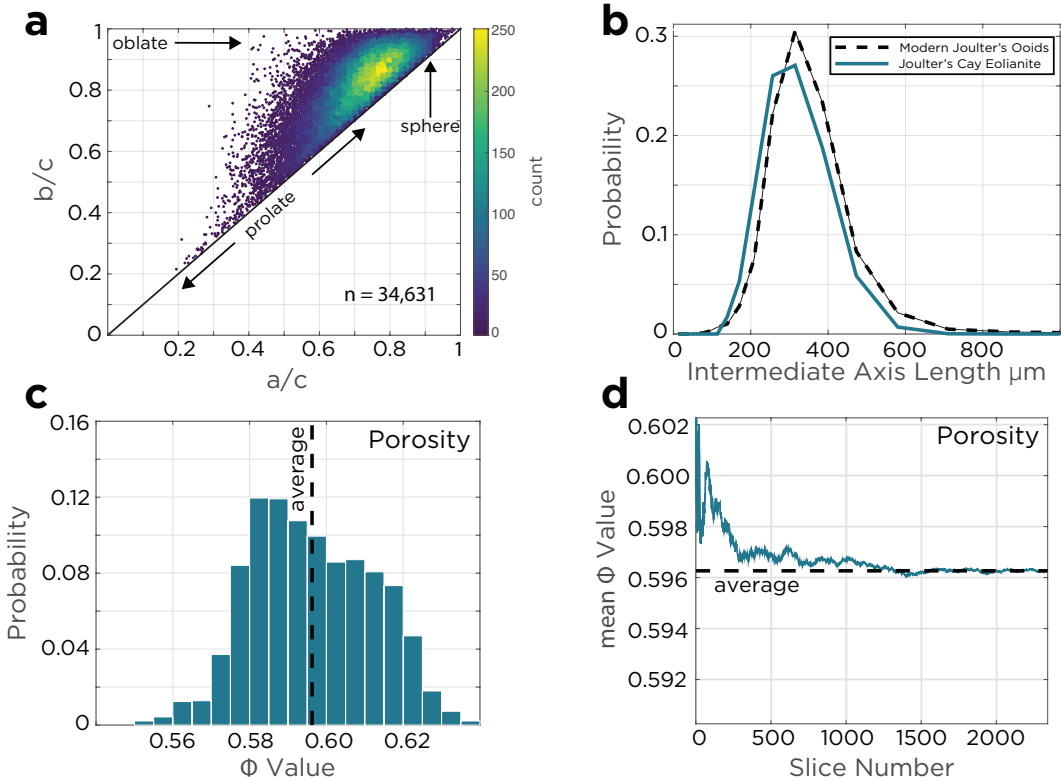


**Figure 6.** (a) A scatter plot of  $b/c$  vs.  $a/c$  for a Holocene oolite from Joulters Cay, Andros Island, The Bahamas. (b) The similarity of major axis length from modern ooid samples from Andros Island (measured by a Beckman Coulter particle size analyzer) and the grain size distribution from the Joulters Cay sample suggests that the image processing routine is accurately measuring ooid size. (c) In this sample, 2D porosity estimates from an individual 2D slice span 7%. The true porosity value from the 3D reconstruction is 59.6% (d). It took over 1200 slices for the running mean to converge on the correct porosity value (There are more than 847 slices in the 3D volume because of the resampling to make the voxels equidimensional).

## 206 4 Growth History

207 Previous studies have outlined a method for reconstructing paleohydraulic conditions  
 208 from the growth histories of ooids (Heller et al., 1980; Sipos et al., 2018), but the  
 209 studies have been hindered by the 2D data available. With serial sections from GIRI,  
 210 we are able to reconstruct growth histories in three dimensions by tracing a single lam-  
 211 ination on dozens of slices. From these traces, we build a model of the cortex and mea-  
 212 sure the dimensions of an ooid as it grows.

213 An ooid grows through the precipitation of calcium carbonate on its cortex, which  
 214 leads to surface normal growth. The evolution of ooid shape as a function of surface nor-  
 215 mal growth can be modeled with equation 1 (Trower et al., 2018):

$$\left(\frac{a}{c}\right)_{new} = \frac{axis_{minor} + x}{axis_{major} + x} \quad \text{and} \quad \left(\frac{a}{b}\right)_{new} = \frac{axis_{intermediate} + x}{axis_{major} + x} \quad (1)$$

216 This equation allows us to model how ooid shape evolves as a function of the ini-  
 217 tial shape in the absence of abrasion (dashed lines in Figure 7), and attribute deviations  
 218 from this growth model to abrasion (Trower et al., 2018). For example, in modern stud-  
 219 ies of ooids in Turks and Caicos, ooids become more spherical than surface normal pre-  
 220 cipitation predicts because abrasion rounds the ooid as it is transported via saltation (Trower  
 221 et al., 2018).

### 222 4.1 Application of Growth History to Giant Ooids

223 Giant ooids are exceptionally large (> 2 mm) and rare in the stratigraphic record,  
 224 but are abundant during the Neoproterozoic Era and in the aftermath of the end-Permian  
 225 mass extinction (Li et al., 2013), two intervals that are unusual and important for un-  
 226 derstanding marine response to major environmental perturbations. The formation of  
 227 giant ooids requires unique ocean conditions including some combination of increased  
 228 precipitation rate of calcium carbonate, increased transport of ooids (i.e. faster current  
 229 velocities), decreased abrasion from less mass (organic cores), and/or decreased supply  
 230 of nuclei for ooid genesis (Sumner & Grotzinger, 1993).

231 We made 3D reconstructions of giant ooids from the Triassic Great Bank of Guizhou  
 232 in China to determine if the growth history of the giant ooids contain clues about the  
 233 chemical and hydrological conditions that lead to their formation. We found that as the  
 234 giant ooids grew, they tend towards a more spherical shape, which is the expected re-  
 235 sult of surface normal growth and/or transportation by saltation. However, this long term  
 236 trend toward increased sphericity was punctuated by abrasion and fragmentation events  
 237 that led to short term deviations toward prolate or oblate shapes. (Figure 7a).

238 The observation of fragmentation events in the growth history of these giant ooids  
 239 (Figure 7a), and the absence of organic cores eliminates the hypothesis that giant ooids  
 240 were able to grow because of decreased abrasion due to less mass. Three-dimensional re-  
 241 constructions of giant ooids can help distinguish between the remaining hypotheses be-  
 242 cause serial grinding and imaging allows us to definitively determine the composition of  
 243 the nucleus in thousands of ooids per sample, and the evolution of ooid shape as it grows  
 244 will provide clues about the environmental conditions that produced giant ooids. For ex-  
 245 ample, if ooids follow a surface normal growth path, then giant ooids probably formed  
 246 formed because of increased precipitation rate of calcium carbonate, or if ooids transi-  
 247 tion from spherical to prolate at a particular size, we could use this change in transport  
 248 mode to estimate water velocities on in giant-ooid-forming environments (Sipos et al.,  
 249 2018).

250 Ultimately, solving the enigma of giant ooids will require the analysis of giant ooid  
 251 growth histories from ooids on many ancient platforms. But it is crucial that these re-

252 constructions are made in 3D because estimates of the growth history of an ooid based  
 253 on 2D intersections are unreliable. By measuring the aspect ratio of each growth band  
 254 on a randomly-oriented plane intersecting the 3D reconstruction, we simulate the appar-  
 255 ent growth history of one of these giant ooids (green ooid from Figure 7a) as recorded  
 256 by 2D intersections. We find that 2D growth histories of the same ooid can show an alarm-  
 257 ing range of growth histories, including a few that suggest a decrease in the aspect ra-  
 258 dio despite the 3D reconstruction showing this ooid became much more spherical as it  
 259 grew (Figure 7c). If we assume the ooid from the 2D intersection is prolate and then cal-  
 260 culate the the change in sphericity as it grows, we find that the 2D growth histories sys-  
 261 tematically underestimate the change in sphericity (Figure 7d). This experiment only  
 262 includes planes that cut through the nucleus, so this result is a minimum-error scenario.  
 263 This systematic error means that analysis of growth histories using 2D intersections would  
 264 undervalue the roll of processes that make ooids spherical (i.e., surface normal precip-  
 265 itation and saltation) when trying to understand the environments that made giant ooids.

## 266 5 Conclusions

267 Many studies have argued that ooid size and shape are related to environmental  
 268 conditions. This link between morphology and environment has been modeled both nu-  
 269 mERICALLY and physically (Sumner & Grotzinger, 1993; Sipos et al., 2018; Trower et al.,  
 270 2017), and observed in modern environments (Trower et al., 2018). Ooid morphology has  
 271 the potential to be a powerful tool for interpreting the rock record, but the error asso-  
 272 ciated with 2D measurements drowns out any signal, prohibiting application to the strati-  
 273 graphic record. By measuring ooid morphology in 3D, we can begin to sharpen our in-  
 274 terpretations of the ancient rock record, and fully utilize the potential of ooids as envi-  
 275 ronmental indicators across Earth's history.

## 276 Acknowledgments

277 This paper benefited from feedback by E. Geyman and R. Manzuk. We thank D. Lehrmann  
 278 and J. Payne for providing the sample from the Great Guizhou Bank. S. Ravi and I. Buynevich  
 279 generously allowed us to use their laser particle analyzer and camsizer, respectively. G.  
 280 Lobet assisted with lab work. This work was supported by NSF Earth Sciences Grant  
 281 1028768 to A. Maloof. Code and data are available at <https://github.com/boltonhowes22/Ooid-Morphometrics>, and full resolution images are available upon request.

## 283 References

- 284 Bathurst, R. G. (1972). *Carbonate Sediments and their Diagenesis*. (Vol. 12). Else-  
 vier.
- 285 Capowiez, Y., Pierret, A., & Moran, C. J. (2003). Characterisation of the three-  
 dimensional structure of earthworm burrow systems using image analysis and  
 mathematical morphology. *Biology and Fertility of Soils*, 38(5), 301–310.
- 286 DeHoff, R. (1983). Quantitative serial sectioning analysis: Preview. *Journal of Mi-  
 croscopy*, 131(3), 259–263.
- 287 Domokos, G., & Gibbons, G. (2012). The evolution of pebble size and shape in  
 space and time. *Proc. R. Soc. A*, rspa20110562.
- 288 Geyman, E. C., & Maloof, A. C. (2018). How do carbonates record seawater chem-  
 istry? The Bahamas as a modern analogue for climate records preserved in  
 ancient shallow-water carbonates. *GSA Annual Meeting*.
- 289 Halley, R. B., & Harris, P. M. (1979). Fresh-water cementation of a 1,000-year-old  
 oolite. *Journal of Sedimentary Research*, 49(3), 969–987.
- 290 Harris, P., Diaz, M. R., & Eberli, G. P. (2019). The formation and distribution of  
 modern ooids on Great Bahama Bank. *Annual review of marine science*, 11,  
 491–516.

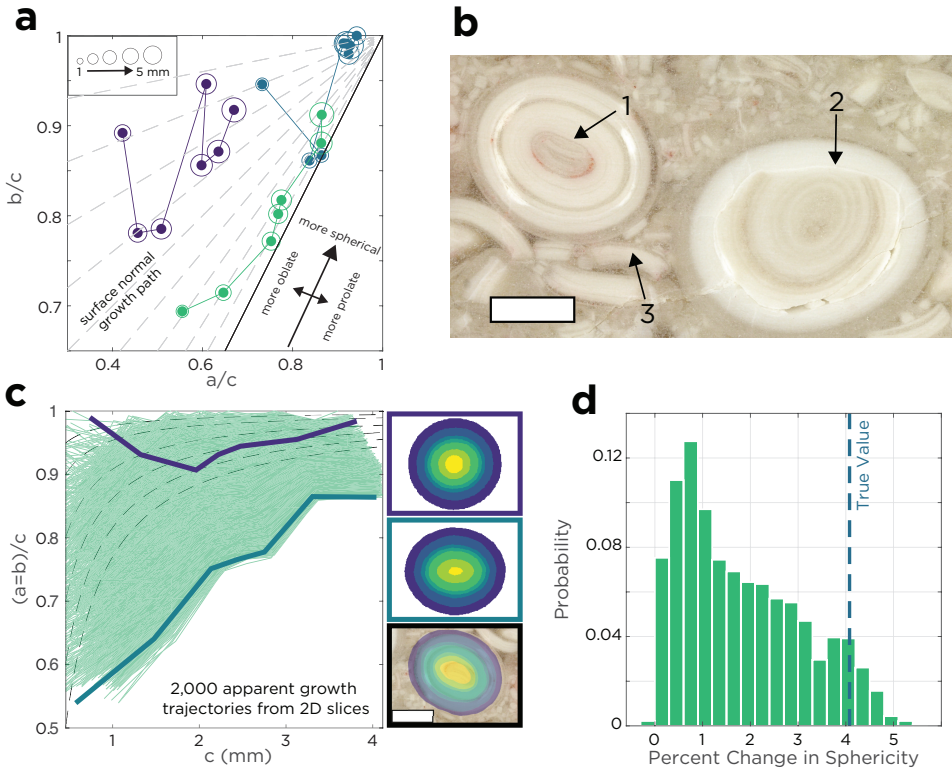


**Figure 7.** (a) Growth histories of three Triassic giant ooids from the Great Bank of Guizhou show ooids becoming more spherical as they grow (although punctuated by abrasion events that increase short-term prolateness or oblateness). (b) Oolite with giant ooids from Great Bank of Guizhou. (1) fragment of giant ooid as nucleus for a different giant ooid, (2) Abrasion/fracture surface on giant ooid overgrown by calcium carbonate, and (3) giant ooid fragments in the matrix of the oolite. Scale bar is 2 mm. (c) The green lines are 2,000 simulated growth histories of the ooid in green if the data were collected from 2D intersections. (d) Percent change in the sphericity ( $\Psi = \frac{\pi^{\frac{1}{3}} 6(V_p)^{\frac{2}{3}}}{A_p}$ , where  $V_p$  is the volume of the particle and  $A_p$  is the surface area of the particle) of the ooid from the first growth band to the last growth band. The histogram is of all the apparent growth paths from (b), and assuming the ooid is prolate, as opposed to oblate. For reference, the sphericity of a sphere is 1 and the sphericity of a cube is 0.806. The true value line is made from the 3D reconstruction.

- 301 Heller, P. L., Komar, P. D., & Pevear, D. R. (1980). Transport processes in ooid  
302 genesis. *Journal of Sedimentary Research*, 50(3).
- 303 Higgins, M. D. (2000). Measurement of crystal size distributions. *American Mineral-  
304 ogist*, 85(9), 1105–1116.
- 305 Jaquet, C., Andó, E., Viggiani, G., & Talbot, H. (2013). Estimation of separating  
306 planes between touching 3D objects using power watershed. In *International  
307 symposium on mathematical morphology and its applications to signal and  
308 image processing* (pp. 452–463).
- 309 Li, F., Yan, J., Algeo, T., & Wu, X. (2013). Paleoceanographic conditions follow-  
310 ing the end-Permian mass extinction recorded by giant ooids (moyang, south  
311 china). *Global and Planetary Change*, 105, 102–120.
- 312 MacLennan, S., Park, Y., Swanson-Hysell, N., Maloof, A., Schoene, B., Gebreslassie,  
313 M., ... Haileab, B. (2018). The arc of the snowball: U-pb dates constrain  
314 the islay anomaly and the initiation of the sturtian glaciation. *Geology*, 46(6),  
315 539–542.
- 316 Mariotti, G., Pruss, S., Summons, R., Newman, S., & Bosak, T. (2018). Contribu-  
317 tion of benthic processes to the growth of ooids on a low-energy shore in Cat  
318 Island, The Bahamas. *Minerals*, 8(6), 252.
- 319 Mehra, A., & Maloof, A. (2018). Multiscale approach reveals that Cloudina ag-  
320 ggregates are detritus and not in situ reef constructions. *Proceedings of the Na-  
321 tional Academy of Sciences*, 201719911.
- 322 Object Research Systems, Inc. (n.d.). Dragonfly. Retrieved from <http://www.theobjects.com/dragonfly>
- 324 Peterson, T. D. (1996). A refined technique for measuring crystal size distributions  
325 in thin section. *Contributions to Mineralogy and Petrology*, 124(3-4), 395–405.
- 326 Pierret, A., Capowiez, Y., Belzunges, L., & Moran, C. (2002). 3d reconstruction  
327 and quantification of macropores using x-ray computed tomography and image  
328 analysis. *Geoderma*, 106(3-4), 247–271.
- 329 Rose, C. V., Maloof, A. C., Schoene, B., Ewing, R. C., Linnemann, U., Hofmann,  
330 M., & Cottle, J. M. (2013). The end-Cryogenian glaciation of South Australia.  
331 *Geoscience Canada*, 40(4), 256–293.
- 332 Sahagian, D. L., & Proussevitch, A. A. (1998). 3D particle size distributions from  
333 2D observations: stereology for natural applications. *Journal of Volcanology  
334 and Geothermal Research*, 84(3-4), 173–196.
- 335 Sipos, A. A., Domokos, G., & Jerolmack, D. J. (2018). Shape evolution of ooids: a  
336 geometric model. *Scientific Reports*, 8(1), 1758.
- 337 Sumner, D. Y., & Grotzinger, J. P. (1993). Numerical modeling of ooid size and  
338 the problem of Neoproterozoic giant ooids. *Journal of Sedimentary Research*,  
339 63(5).
- 340 Trower, E. J. (2020). The enigma of neoproterozoic giant ooids—fingerprints of ex-  
341 treme climate? *Geophysical Research Letters*, e2019GL086146.
- 342 Trower, E. J., Cantine, M. D., Gomes, M. L., Grotzinger, J. P., Knoll, A. H., Lamb,  
343 M. P., ... others (2018). Active ooid growth driven by sediment transport in a  
344 high-energy shoal, Little Ambergris Cay, Turks and Caicos Islands. *Journal of  
345 Sedimentary Research*, 88(9), 1132–1151.
- 346 Trower, E. J., Lamb, M. P., & Fischer, W. W. (2017). Experimental evidence  
347 that ooid size reflects a dynamic equilibrium between rapid precipitation and  
348 abrasion rates. *Earth and Planetary Science Letters*, 468, 112–118.